

## Article

# Optimization of the Effect of Laser Power Bed Fusion 3D Printing during the Milling Process Using Hybrid Artificial Neural Networks with Particle Swarm Optimization and Genetic Algorithms

Husam Kaid <sup>1,\*</sup>, Abdulmajeed Dabwan <sup>1,\*</sup>, Khaled N. Alqahtani <sup>1</sup>, Emad Hashiem Abualsaoud <sup>1</sup>, Saqib Anwar <sup>2</sup>, Ali M. Al-Samhan <sup>3</sup> and Abdullah Yahia AlFaify <sup>2</sup>

<sup>1</sup> Industrial Engineering Department, College of Engineering, Taibah University, Medinah 41411, Saudi Arabia; knqahtani@taibahu.edu.sa (K.N.A.); eabualsaoud@taibahu.edu.sa (E.H.A.)

<sup>2</sup> Industrial Engineering Department, College of Engineering, King Saud University, P.O. Box 800, Riyadh 11421, Saudi Arabia; sanwar@ksu.edu.sa (S.A.); aalfaify@ksu.edu.sa (A.Y.A.)

<sup>3</sup> Industrial Engineering Department, College of Engineering and Architecture, Alyamamah University, Riyadh 11512, Saudi Arabia; a\_alsamhan@yu.edu.sa

\* Correspondence: hkaid@taibahu.edu.sa (H.K.); adabwan@taibahu.edu.sa (A.D.)

**Abstract:** Additive manufacturing (AM) is gaining popularity as it can produce near-net geometries and work with difficult-to-manufacture materials, such as stainless steel 316L. However, due to the low surface quality of AM parts, machining and other finishing methods are required. Laser powder bed fusion (LPBF) components can be difficult to finish as the surface roughness ( $S_a$ ) can vary greatly depending on the part's orientation, even when using the same machining parameters. This paper explored the effects of finishing (milling) SS 316L LPBF components in a variety of part orientations. The effect of layer thickness (LT) variation in LPBF-made components was also studied. LPBF parts of 30, 60, 80, and 100  $\mu\text{m}$  layer thicknesses were created to analyze the effect of the LT on the final milling process. Additionally, the effect of cutting speed during the milling process on the surface roughness of the SS 316L LPBF component was investigated, along with the orientations and layer thicknesses of the LPBF components. The results revealed that the machined surface undergoes significant orientation and layer thickness changes. The investigations employed a factorial design, and analysis of variance (ANOVA) was used to analyze the results. In addition, an artificial neural network (ANN) model was combined with particle swarm optimization (denoted as ANN-PSO) and the genetic algorithm (denoted as ANN-GA) to determine the optimal process conditions for machining an SS 316L LPBF part. When milled along (Direction B) an orientation with a cutting speed of 80  $\text{m}/\text{min}$ , the LPBF component produced, with a layer thickness of 60  $\mu\text{m}$ , achieves the lowest surface roughness. For instance, the  $S_a$  of a milled LPBF part can be as low as 0.133  $\mu\text{m}$ , compared to 7.54  $\mu\text{m}$  for an as-fabricated LPBF part. The optimal surface roughness was 0.155  $\mu\text{m}$  for ANN-GA and 0.137  $\mu\text{m}$  for ANN-PSO, whereas the minimal surface roughness was experimentally determined to be 0.133  $\mu\text{m}$ . Therefore, the surface quality of both hybrid algorithms has improved, making them more efficient.

**Keywords:** SS 316L; additive manufacturing; laser powder bed fusion; layer thickness; surface roughness; particle swarm optimization; genetic algorithm; artificial neural networks



**Citation:** Kaid, H.; Dabwan, A.; Alqahtani, K.N.; Abualsaoud, E.H.; Anwar, S.; Al-Samhan, A.M.; AlFaify, A.Y. Optimization of the Effect of Laser Power Bed Fusion 3D Printing during the Milling Process Using Hybrid Artificial Neural Networks with Particle Swarm Optimization and Genetic Algorithms. *Processes* **2023**, *11*, 2892. <https://doi.org/10.3390/pr1102892>

Academic Editors: Maximilian Lackner, Cayetano Espejo Conesa and Haoqi Zhang

Received: 24 August 2023

Revised: 20 September 2023

Accepted: 27 September 2023

Published: 30 September 2023



**Copyright:** © 2023 by the authors. Licensee MDPI, Basel, Switzerland. This article is an open access article distributed under the terms and conditions of the Creative Commons Attribution (CC BY) license (<https://creativecommons.org/licenses/by/4.0/>).

## 1. Introduction

Stainless steel 316L has several applications in aerospace and the food industry. Austenitic stainless steels are also widely utilized in a variety of industries [1], from aviation to nuclear power to defense to the food industry [2] and automotive industry [3], due to their strong resistance to corrosion in high-temperature water and oxidation [4]. The excellent combination of mechanical strength and corrosion resistance of SS 316L has made

it a popular material for reusable medical devices [5]. Poor machinability, however, makes it a typical hard-to-cut material [6]. It has been more obvious in recent years that machining operations (surface grinding, surface milling, surface turning, and surface buffing) [7] that alter the workpiece surface and other finite element numerical procedures [8] have a substantial impact on the surface integrity and corrosion resistance of SS 316L [9]. In conjunction with laser powder bed fusion (LPBF), SS 316L can affordably support individualized implants or prostheses [10]. It is important to pay close attention to the surface properties of these implants due to their communication with the human body. However, L-PBF components are notorious for their low-quality surfaces [11]. The surface characteristics of SS 316L components made with LPBF can be greatly improved through machining. Accordingly, to obtain the appropriate surface quality, extensive work on the machinability of SS 316L LPBF parts is needed.

Additive manufacturing (AM) enables the rapid production of complex-shaped items that cannot be made using traditional machining techniques [12]. Due to these benefits, the biomedical, aerospace, and automotive industries favor this technique [13]. Laser powder bed fusion (LPBF) is a top AM technique for creating a pore gradient structure in 316L stainless steel [14], combining and assembling various powder materials to create customized products [15]. These parts frequently exhibit process-induced micropores and elevated residual stresses [16]. LPBF has great material strength, as it can be completely melted to a 100% density, yet several problems must be solved before rapid manufacturing can be implemented. Part orientation, layering strategy, support generation and structure, process speed, and control facilities are the main challenges [17]. Using the heat from a focused laser beam, powder particles are bonded to one another layer by layer, resulting in dense, functioning objects with intricate geometries [18]. Modern medical implants, including 316L stainless steel bone implants, are made using LPBF. LPBF has several benefits over traditional machining; however, its poor surface quality is a drawback [18,19]. The “stair step” effect, caused by layered approximations of curves and inclined surfaces, impacts surface quality [20]. This is a natural consequence of additive layer deposition and manufacturing in all techniques. Thus, the industrial sector is currently using hybrid production methods, such as AM and final machining. The surface quality and performance of additively generated parts can be enhanced through finish machining [13].

To obtain desirable mechanical properties from LPBF-made 316L SS, several processing parameters are optimized. Layer thickness affects the cooling, mass transfer, building, and heat transfer rates [21]. An increase in (powder) layer thickness shortens production, whereas a reduction yields denser, more precisely sized products [22]. The minimum layer thickness ( $20\text{ }\mu\text{m}$ ) was determined for the best material density [23]. Correct component thickness is crucial for intended shape, performance, and characteristics [24]. This research altered the LPBF process parameters and layer thickness to enhance the SS 316L component’s surface roughness. Strano et al. [20] analyzed the upper surfaces of SS 316L LPBF components at various angles in order to determine the main factors contributing to surface roughness. These findings highlighted that layer thickness is more important than particle size in determining surface roughness, and that step edge sharpness and partially bound particles on top of surfaces should be considered. Souza et al. [24] investigated how processing parameters impact LPBF steel component hardness, microstructure, porosity, and roughness. A 400 W laser with high power improved the process energy, potentially shortening production times and cutting costs. The optimal LPBF parameters were determined and utilized to produce a new lot of steel components to study how a part built orientation on a substrate affects its mechanical properties. Mechanical properties were most sensitive to component porosity. To compare production times and LPBF settings, they conducted some basic studies. Tain et al. [25] analyzed how process parameters affected LPBF part surface quality. Increased laser power and decreased scan rate reduced balling and improved surface quality. Guo et al. [26] found that hatch spaces exceeding  $45\text{ }\mu\text{m}$  result in rougher surfaces, but decrease with a lower laser power or slower scan speed. Zhang et al. [27] measured fused section surface roughness and average height drops

on-site using digital fringe projection. Yeung et al. [28] adjusted laser power based on part shape to improve LPBF surface quality. Although research has modified process parameters *in situ*, surface roughness still requires a secondary operation, such as machining.

Finishing (typically machining) is necessary for LPBF components to attain the appropriate surface quality and performance [20]; surface quality is improved during the milling of LPBF-produced parts compared to standard parts. [29]. Furthermore, different orientations of stainless steel 316L parts during milling have varying degrees of surface roughness due to the influence of LPBF manufacturing [30]. Surface roughness is affected by machining and must be within acceptable limits to meet clinical standards [31]. Finishing is necessary for EBM parts as well [32]; the milling process affects the surface roughness of EBM  $\gamma$ -TiAl components in different ways depending on their orientation [33]; the machinability of the EBM  $\gamma$ -TiAl part on a surface finish led to poor surface integrity with coated carbide inserts compared to uncoated carbide inserts [34]. In contrast, there is scant information available on the machining of LPBF components. The work of Kaynak and Kitay [13] focused on using a variety of feed rates and cutting speeds to achieve a dry finish in the machining of SS 316L parts produced via additive manufacturing. The surface roughness of the SS 316L LPBF component was found to have decreased by as much as 88% after finishing machining. It also had a major impact on the LPBF components' microstructure and microhardness, resulting in finer grains and a strain-hardened layer on the surface and inside of the part. Finish machining also dramatically reduced the surface and subsurface porosity density in comparison to an as-fabricated part. Secondary machining characteristics were analyzed for both wrought and SS 316L LPBF by Polishetty et al. [35] so that the desired surface and shape could be attained. They wrapped up by making the point that wrought components are easier to machine than SS 316L LPBF ones. Farooq et al. [36] examined the effects of cutting speed, depth of cut, and feed rate regarding the surface roughness and tool life for the SS 316L LPBF component throughout the turning process. The tool life improvement objectives were met at a rate of 100%, while the surface roughness objectives were met at a rate of 98.95%. Struzikiewicz et al. [37] reported data on the total cutting force, maximum temperature, and surface roughness for the turned SS 316L LPBF part. Using the Taguchi technique, they devised statistical analysis for the test findings. Their results showed that the feed rate has a major impact on the cutting force values, that the cutting speed and feed rate have a major impact on the surface roughness, and that the feed rate and cutting speed have a major impact on the maximum average temperature.

Some studies have shown that the 3D printing layer orientations considerably affect the final visual appearance of the additively manufactured parts. Milling of the Ti6Al4V [38] and  $\gamma$ -TiAl EBM [33] components and turning of the Ti6Al4V EBM [39] components are examples where the effects of layer orientations have been studied and published. It has been found through investigations that the same machining parameters can produce varying degrees of surface roughness depending on the orientation of the EBM component being machined [40]. Heat treatment helped reduce the effect of part orientation on EBM Ti6Al4V components [41]. Another investigation [30] examined the impact on milling orientations of changing the layer thickness during the LPBF manufacturing of SS 316L components. However, no study has been found as of yet that optimizes the effects of layer orientation on finishing the LPBF component.

In order to improve the surface quality of an additively manufactured product during the milling process, it is always advantageous to understand the impact of varying the input process parameters. For printed products to have a high-quality surface, the milling process needs highly experienced operators; it is also costly and requires significant trial and error. Thus, the purpose of this study was to find the optimal combination of milling process settings considering part orientation and layer thickness for printed products. ANNs are excellent tools for manufacturing processes with complicated and nonlinear relationships between the input and output variables. ANNs have been useful for modeling [42], analyzing, optimizing [43], and predicting engineering problems, such

as manufacturing [44], welding [45,46], and 3D printing processes [47]. Giri et al. [48] developed an ANN to predict the surface roughness, tensile strength, and build time of polylactic acid (PLA) produced via fused deposition modeling (FDM). The optimization results indicated that their ANN can predict experimental data with a correlation coefficient of  $R = 0.99837, 0.9981$ , and  $0.9984$ , respectively, for surface roughness, tensile strength, and build time, and with root mean square error values of  $0.241, 0.5543$ , and  $0.578$  for the three outputs. Shirmohammadi et al. [49] investigated the impact of various process conditions in FDM 3D printing on the surface roughness of printed parts. They used two different methods, including the response surface methodology (RSM) and a hybrid algorithm that combined an ANN and the PSO algorithm. The results of their optimization demonstrated that both the RSM and the hybrid algorithm are capable of accurately estimating the optimal parameters, with a relative error of less than 10%. Soler et al. [50] constructed an ANN to estimate the surface roughness of Ti6Al4V alloy specimens produced via selective laser melting (SLM) after finishing through blasting and electropolishing methods. The optimal result was achieved using a sequential combination of two optimization techniques. First, the GA was applied to find the best blasting and electropolishing parameters; then, this initial optimization was used as a starting point for a nonlinear optimization method. The optimization algorithm provided the parameters to be implemented to minimize surface roughness by approximately 60%. Saad et al. [51] introduced the effect of various process conditions on the surface roughness of printed parts produced via FDM 3D printing. Two optimization methods were used to minimize the surface roughness, namely the RSM and a hybrid algorithm that combined an ANN and the symbiotic organism search (SOS), referred to as ANN-SOS. The optimization results indicated that ANN-SOS achieved a minimal surface roughness of roughly  $2.011 \mu\text{m}$ , 12.36% better than the RSM approach.

According to the findings of these investigations, it is not possible to foresee how LPBF methods will affect the machinability of the material, and each LPBF process will have its own distinct effect on the additively created components. As a result, more work needs to be put into analyzing how different LPBF methods affect material machinability. One of the most critical machinability techniques in LPBF is the use of alternative part orientations. Few researchers have attempted to address the challenge of milling AM components while taking part orientations into account. The purpose of this study was to identify how changing the part orientation (direction), layer thickness, and cutting speed during milling affects the surface roughness of LPBF SS 316L parts. In addition, an ANN with GA and PSO was used to optimize the impact of the LPBF process on the machinability of SS 316L, leading to a better-machined surface.

## 2. Methodology

### 2.1. Material Details

The LPBF technique was used to create an SS 316L component with a size of  $10 \times 10 \times 10 \text{ mm}^3$ . Layer thicknesses (LTs) were varied across the four samples that were created. The SS 316L powder (Maher, Sheffield, UK) had spherical grains that ranged in size from  $15$  to  $45 \mu\text{m}$ . Table 1 displays the elements that compose the 316L SS powder. The LPBF machine used was a Renishaw UK AM250 type from Gloucester, UK, which utilized a laser-pulsed beam with a power output of  $200 \text{ W}$ . The unit had a build volume capacity of  $250 \times 250 \times 300 \text{ mm}^3$  and a laser beam diameter of  $70 \times 5 \mu\text{m}$ . When performing LPBF, the scan approach employed was called “Meander”, and it involved a layer-by-layer rotation of 67 degrees in the scan direction [52]. The build platform was preheated to  $170^\circ\text{C}$ , in accordance with the manufacturer-recommended standard build procedure, and all builds were fabricated under an Argon atmosphere with an oxygen level below 0.1%. The LPBF’s actual manufactured component is displayed in Figure 1. Table 2 contains the LPBF parameters that were chosen based on previous investigations [30,52]. To examine

the effect of layer thickness alone on machining, the energy density was held constant by varying the exposure time in accordance with Equation (1):

$$\text{Energy density} = (\text{laser power}) / (\text{hatching distance} \times \text{scan speed} \times \text{layer thickness}). \quad (1)$$

**Table 1.** Powdered stainless steel 316L chemistry [30,52].

Element	Cr	Ni	Mo	Mn	Si	Cu	N	O	P	C
Wt. (%)	17.50–18.00	12.50–13.00	2.25–2.50	≤2.00	≤0.75	≤0.50	≤0.10	≤0.10	≤0.025	≤0.030

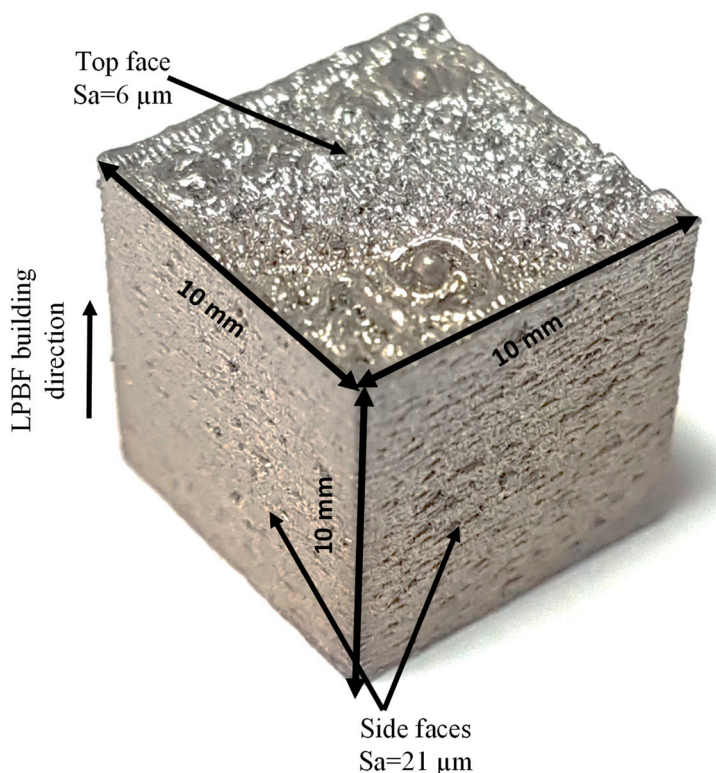


**Figure 1.** A SS 316L block sample produced via LPBF.

**Table 2.** LPBF manufacturing process parameters for SS 316L [30,52].

LPBF Parameter	Value
Energy density	50 J/mm <sup>3</sup>
Point distance	70 μm
Hatching distance	120 μm
Laser power	200 W
Layer thickness	30, 60, 80, 100 μm

Equation (2) can be used to compute the scan speed from the values of point distance (PD), exposure time (ET), and jump speed (JS):

$$\text{Scan speed (SS)} = \text{PD} / (\text{ET} + \text{PD}/\text{JS}) \quad (2)$$

where JS is the speed of the galvanometer mirror as it moves from point to point, which was maintained at 5000 mm/s. Consequently, the scan speed will vary as the ET for each layer thickness varies. For layer thicknesses of 30, 60, 80, and 100 μm, the scan speed was 1093, 564, 402, and 327 mm/s, respectively. Additional information included exposure times of 30, 60, 80, and 100 s for 30, 60, 80, and 100 μm, respectively.

Table 3 shows how the top, side faces, and relative porosity of the as-fabricated parts vary with the layer thickness. While improvements have been made, there are still numerous cases where the surface roughness ratings are excessive. Yasa and Kruth [18] found comparable values of surface roughness. In order to obtain the desired surface finishing on LPBF parts, a secondary procedure is necessary. In this paper, traditional vertical milling was chosen as a supplementary operation to improve surface smoothness. Depending on the desired result, the LPBF part can be machined with a layer thickness of 30, 60, 80, or 100  $\mu\text{m}$ .

**Table 3.** The relative porosity and surface roughness of the as-fabricated components for varying layer thicknesses.

	LT30	LT60	LT80	LT100
Side face ( $\mu\text{m}$ )	11.58	7.54	8.28	9.41
Top side ( $\mu\text{m}$ )	12.37	6.05	9.63	23.09
Relative porosity (%)	4.87	0.97	1.53	3.94

## 2.2. Milling Options and Measurement Setups

In order to obtain the best possible surface roughness while milling LPBF parts, it is crucial that the 3D-printed part is correctly oriented with respect to the tool feed direction (TFD). Tool feed across the layer (Direction A), tool feed parallel to the planes of the layers (Direction B), and tool feed in a layer plane (Direction C) are the three possible machining directions for the LPBF component. The three potential TFD viewing angles are depicted schematically in Figure 2. Figure 3a depicts the tooling and workpiece holding fixture. The cutting tool's geometric dimensions and properties are depicted in Figure 3b. Direction A, Direction B, and Direction C are shown on an actual LPBF component in Figure 3c. In the first stage of milling the samples, a 50 mm/min feed rate, 80 m/min of cutting speed, 6 mm of tool diameter, and 0.4 mm of cutting depth were used. The purpose of this process was to prepare the LPBF components for finishing by removing their uneven and rough surfaces. In order to determine how LPBF component orientation affected milling quality, work was carried out utilizing the process parameters listed in Table 4. Table 4 lists the typical process parameters for milling SS 316L, which agree with results from similar investigations [30,53–55]. The milling tests were carried out on a three-axis numerically controlled machine (Ecoline DMC 635 V from DMG Mori in Oelde, Germany) that is capable of speeds of up to 24 m per minute in feed and 1 micrometer in positioning resolution. A 6 mm diameter solid carbide end mill was employed for the job. The roughness of a surface, denoted by the  $\text{Sa}$  value, was examined as a response. Using a 3D optical profilometer (Germany's Contour GT-K is manufactured by Bruker in Berlin, Germany), the  $\text{Sa}$  of the machined components was measured. A scanning area of 2.2 mm  $\times$  1.7 mm was employed. An optical profilometer utilizes white light interferometry to determine the 3D surface parameter ( $\text{Sa}$ ). The Vision 64 program converts detailed scans into precise 3D representations. Later, the software computed the 3D roughness parameter in accordance with ISO 25178-2 [30,56]. According to Equation (3), the  $\text{Sa}$  parameter is the average height across a certain area. [57]:

$$\text{Sa} = \frac{1}{A} \iint_A A|z(x, y)| dx dy \quad (3)$$

where  $A$  is the area being sampled, and  $z(x, y)$  represents the number of measurement sites.

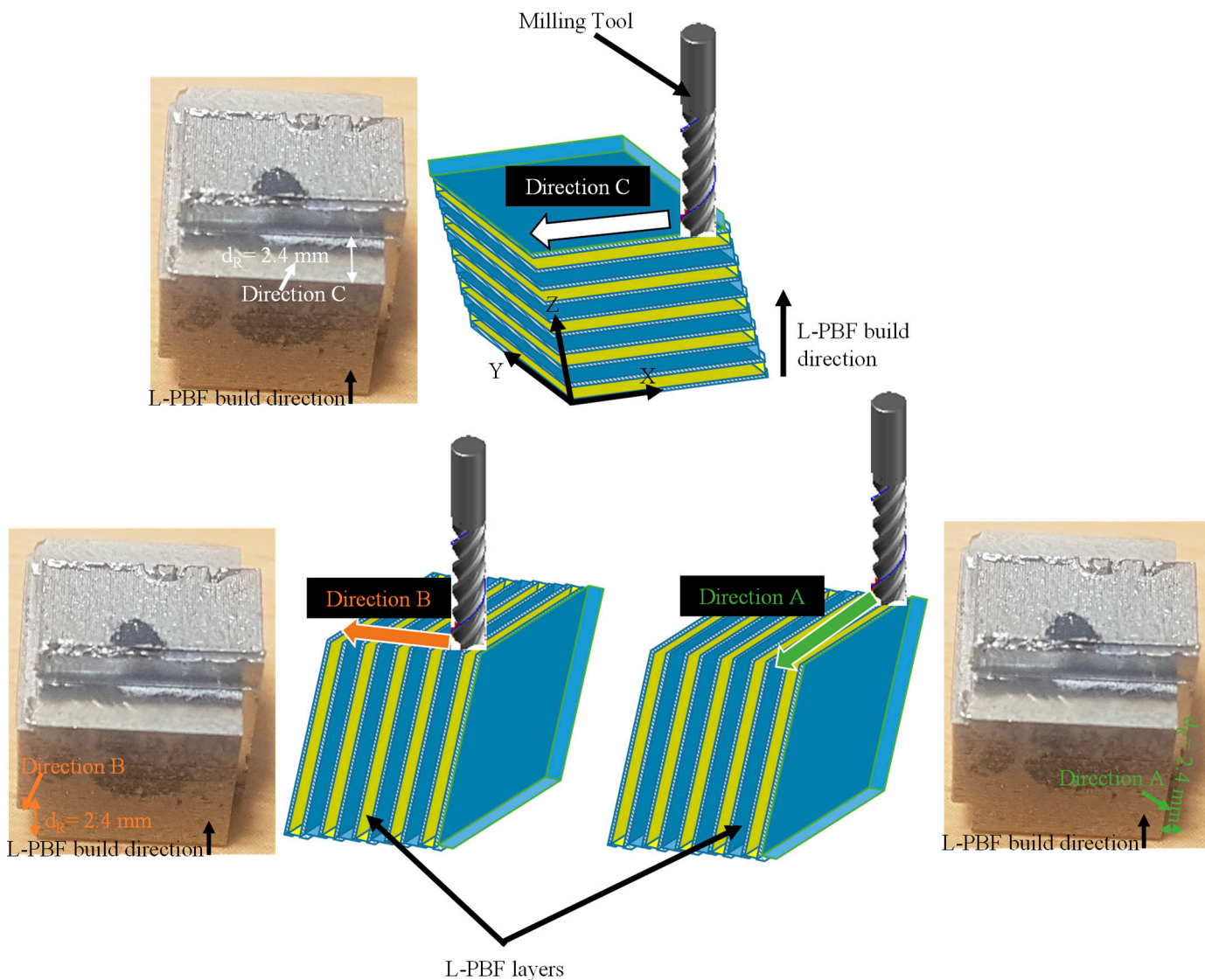


**Figure 2.** Millable orientations of the LPBF component with actual parts. The blue color represents the first layer and the yellow color highlights the next layer, and so on, while the dashed lines represent the bonded layers.

**Table 4.** The parameters for milling the LPBF component.

Parameter	Values
Cutting speed, (V) m/min	80, 120
Feed rate, (f) mm/min	50
Depth of cut, (d) mm	0.4
Radial depth of cut, (dR) mm	2.4
Tool feed direction, (TFD)	Direction A, Direction B, and Direction C
Layer thickness, (LT) $\mu\text{m}$	30, 60, 80, 100

After milling, in the center of the milled zone along the feed direction, five portions of 2.2 mm and 1.7 mm were scanned for each of the three orientations (Direction A, Direction B, and Direction C). The roughness of the surface was determined by taking the mean of five readings obtained in each direction.

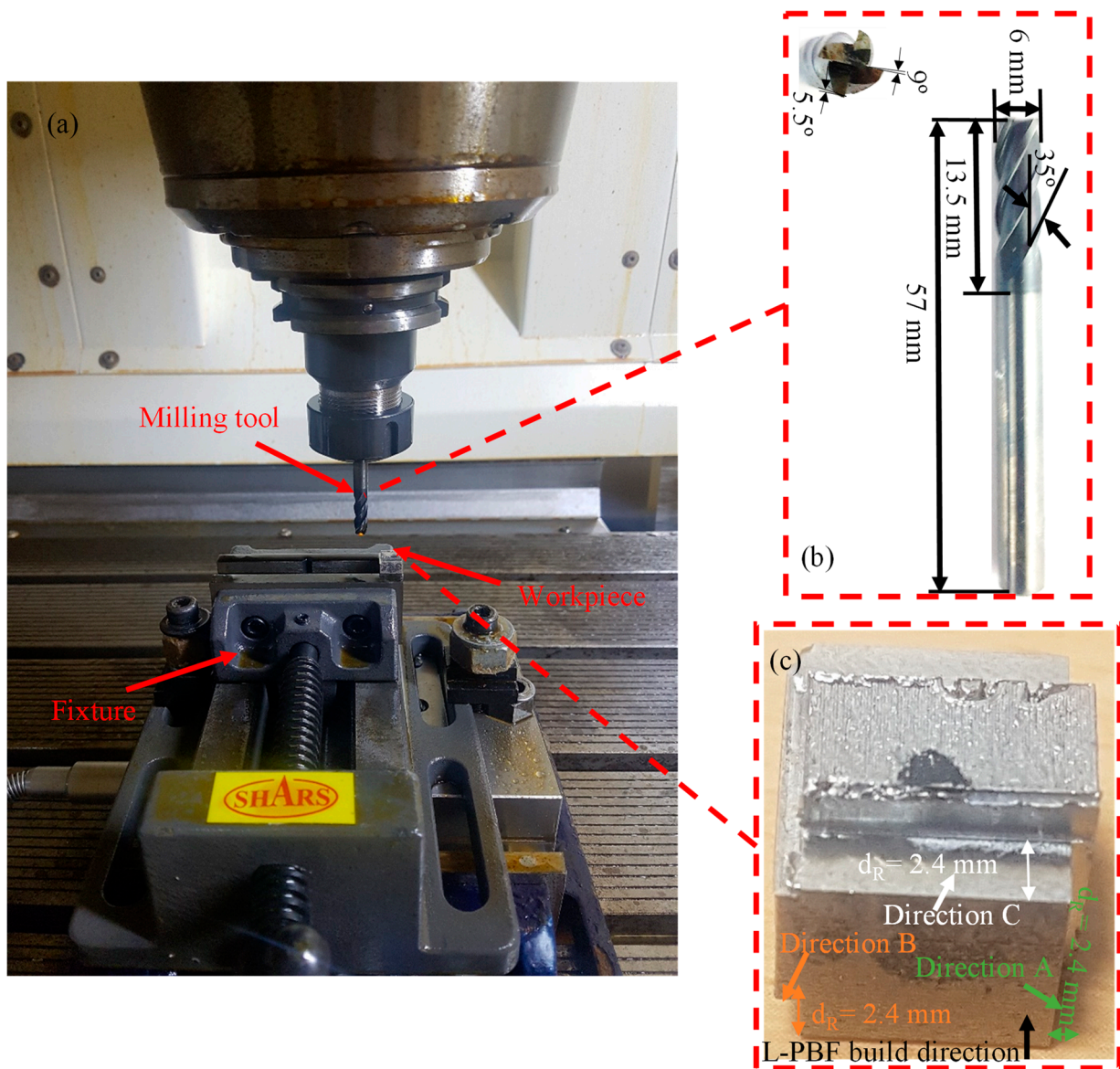


**Figure 3.** (a) Experimental setup. (b) Magnification of the cutting tool. (c) Magnification of the milled sample.

### 2.3. Artificial Neural Networks

The artificial neural network (ANN) is commonly used as a predictive model for estimating output values based on various input factors. The paradigm of human minds learning from experience serves as inspiration for ANNs. ANNs consist of multiple layers, each containing a specific number of neurons. In the context of fully connected ANNs, it has been observed that every neuron inside a given layer receives input signals from all neurons in the preceding layers. There are three different types of layers. The input layer (i) consists of neurons responsible for receiving the initial data ( $x$ ) and transmitting it to the neurons in the hidden layers (ii) for subsequent processing. These signals transmit information to the neurons in the output layer (iii), which ultimately generates the output value ( $y$ ) [58,59]. Each neuron possesses weights ( $w$ ) and a bias ( $b$ ), which are modified during the process of training, as well as a transfer function.

In general, the numerical values of these weights are determined through the iterative training of ANNs with the objective of minimizing the loss function that measures the difference between the predicted values and actual output values. Back propagation, a

widely utilized method for weight optimization, implements the chain rule to iteratively compute gradients for each layer [60]. Following the completion of training, ANNs have the capability to generate outputs through utilizing the values of the hidden inputs. The structure of an ANN typically contains four important subcomponents, which are the number of “hidden layers”, the number of “neurons” in each layer, the “activation function”, and the “loss estimation function”. Figure 4 shows a visual representation of the ANN.

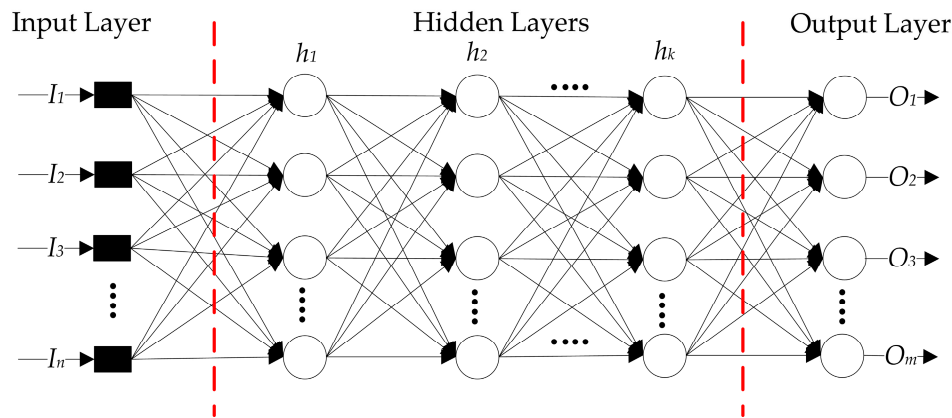


**Figure 4.** A typical diagram of the ANN.

The calculation of the network’s performance and the accuracy of the predictions involves using the root mean square error (RMSE), a statistical measure that quantifies the significant gap between the experimental and predicted values. The RMSE can be expressed as:

$$RMSE = \sqrt{\frac{\sum_{i=1}^n (y_{i,Pred} - y_{i,Exp})^2}{n}} \quad (4)$$

where  $n$  represents the total number of data points, and  $y_{i,Exp}$  and  $y_{i,Pred}$  denote the experimental and predicted values of experiment  $i$ , respectively ( $i = \{1, 2, 3, \dots, n\}$ ,  $n > 0$ ). The RMSE cannot accurately measure error variables, such as the mean error. However, it provides the benefit of penalizing models that make highly incorrect estimations in specific assessments, as it assesses the squared values of the errors rather than the errors themselves. Thus, it is argued that the RMSE is a more suitable metric than the mean error in this research. This is because a prediction of surface roughness that significantly deviates from the actual value may result in the manufacturing of a component that fails to meet the end user’s requirements [61].

The network’s learning rate was set to values that generated the best correlation coefficient ( $R^2$ ) for the ANN. The constructed model’s fitness can also be expressed via the  $R^2$  value, which can be formulated as follows:

$$R^2 = 1 - \frac{\sum_{i=1}^n (x_i - y_i)^2}{\sum_{i=1}^n (x_i - x_{mean})^2} \quad (5)$$

where  $x_i$  and  $y_i$  denote the target and estimated values for the  $i$ th data point, respectively, and  $x_{mean}$  represents the mean  $x_i$  values.

When designing an ANN, identifying the number of neurons in the hidden layer is an essential step [62,63]. On the one hand, a few neurons in the hidden layer may influence the convergence rate of the network. A large number of neurons can lead to a complex network structure, an increase in training frequency, model overfitting, and a reduction in generalization [64]. Thus, the determination of the number of neurons in the hidden layer is achieved through the method of trial and error, with the objective of minimizing the gap between the values obtained from experimentation and those predicted using the model.

## 2.4. Hybrid Neural Network Algorithm with PSO and the GA

ANN represents one of the most common models for estimating outputs for a range of input factors. Despite the fact that ANNs have the ability to track the complicated and nonlinear relationship between the independent input and output variables, they have constraints, such as slow learning. Consequently, the application of optimization algorithms, including meta-heuristic algorithms, can substantially enhance the performance of ANNs. Numerous researchers currently integrate ANNs with the GA [64–66], PSO [49,67–70], and modified bat-inspired algorithm (MBA) [71] to find the optimal fitness values for single- or multi-objective optimization problems. In this study, ANN-PSO and ANN-GA hybrid algorithms were applied to find the optimal 3D printing process parameter composition.

### 2.4.1. Genetic Algorithm

Darwin [72] developed the GA based on the theory of evolution and the concept of survival of the fittest. This algorithm creates a random initial population of chromosomes and then optimizes it through a series of operations. Typically, chromosomes are expressed as integer strings. Several procedures, such as reproduction, cross-breeding, and mutation, as well as the solution from the previous population, are used to generate a new population and determine the best possible solution. On the basis of the fitness function, the best chromosomes are preserved during reproduction for the next population. Crossover between two parent strings creates offspring (new solutions) by rearranging genes or the segments of chromosomes. The mutation is a method for increasing population diversity through the random modification of portions of a solution. The motivating conviction is that the incoming population will be superior to the outgoing population. New solutions (offspring) are generated through selecting solutions based on their fitness function. The aforementioned process is iterated until the specific termination condition has been satisfied. Researchers could refer to the articles published by the authors of [73,74] for more details. The general pseudocode of the GA is shown in Algorithm 1.

---

**Algorithm 1:** General pseudocode of the GA.

---

```

Begin
     $j = 1$  and  $MaxIt$ ; /*  $j$  is an integer value,  $j > 0$ , and  $MaxIt$  is the maximum integer number
    of iterations*/
    Initial_Population  $P(j)$ ;
    Calculate  $P(j)$ ;
    while  $j < MaxIt$            do
         $P'(j) = Selection\_Parent P(j)$ ;
        Crossover  $P'(j)$ ;
        Mutate  $P'(j)$ ;
        Calculate  $P'(j)$ ;
         $P(j + 1) = Replace (P(j), P'(j))$ ;
         $j = j + 1$ ;
    end while
end begin
```

---

The function “*Initial\_Population*” is used to generate the initial population of candidate solutions, denoted as  $P$ . The function “*calculate*” is used to find the fitness value of each solution in  $P$ . The *Selection\_Parent* function generates its successor  $P'(j)$  using a selection technique. Next, the processes of recombination and mutation are sequentially employed to achieve diversity in populations. The “*calculate*” function is responsible for evaluating the fitness of every individual in the population  $P'(j)$  in order to determine the most suitable survivors. The aforementioned procedure is executed for a certain number of iterations, denoted as  $MaxIt$ .

#### 2.4.2. Particle Swarm Optimization

The PSO technique was first proposed by Kennedy and Eberhart [75]. Particles in PSO move through the problem space by adhering to the best-moving particles at any given time. Each particle in the problem space maintains track of its point location, assisting in locating the current optimal solution. Following each repetition, particles are evaluated using a fitness function. PSO can arrive at a point of convergence more rapidly than other optimization methods. Calculating the optimal value requires the use of a few parameters. The PSO's efficiency can be improved through reducing the number of particles [76]. The general pseudocode of the PSO is illustrated in Algorithm 2.

**Algorithm 2:** General pseudocode of the PSO.

---

```

Begin
    k = 1;
    Initial_Swarm
    for  $i = 1: S$  do /*  $S$  is the number of particles in the swarm */
        Randomly initialize the position the velocity of particle  $i$ ;
        Initialize the best known position of particle  $i$ :  $p_i \leftarrow x_i$ ;
        if  $f(p_i) < f(\Psi)$  then
            Modify the best-known position of the swarm:  $\Psi \leftarrow p_i$ ;
        end if
    end for
    while  $k < MaxIt$  do
        for each particle  $i = 1: S$  do
            for each dimension  $j = 1: n$  do
                Generate random numbers:  $r_1, r_2 \sim U(0, 1)$ ;
                Modify the velocity of particle  $i$  according to
                 $v_{i,d} \leftarrow w v_{i,d} + c_1 r_1 (p_{i,d} - x_{i,d}) + c_2 r_2 (\Psi_d - x_{i,d})$ ;
            end for
            Modify the position of particle  $i$ :  $x_i \leftarrow x_i + v_i$ ;
            if  $f(x_i) < f(p_i)$  then
                Modify the best-known position of the particle:  $p_i \leftarrow x_i$ ;
                if  $f(p_i) < f(\Psi)$  then
                    Modify the best-known position of the swarm:  $\Psi \leftarrow p_i$ ;
                end if
            end if
             $k = k + 1$ ;
        end for
    end while
end begin

```

---

The notations  $x_i$ ,  $v_i$ , and  $p_i$ , represent the position, velocity, and best-known position of particle  $i$ , respectively.  $\Psi$  denotes the swarm's best-known position. The parameter denoted as “ $w$ ” represents the inertia weight. The variables  $r_1$  and  $r_2$  are random numbers that are uniformly distributed in the interval  $(0, 1)$ .  $c_1$  and  $c_2$  are commonly referred to as the cognitive coefficient and social coefficient, respectively.

### 3. Results and Discussions

Two replications of experimental surface roughness data are shown in Table 5.

**Table 5.** Experimental results for surface roughness (Sa).

No.	Direction	Layer Thickness ( $\mu\text{m}$ )	Cutting Speed (m/min)	Surface Roughness ( $\mu\text{m}$ )
1	A	80	80	0.304
2	C	100	80	0.204
3	A	60	120	0.362
4	B	100	120	0.237
5	A	100	80	0.146
6	B	100	120	0.222
7	C	30	120	0.349
8	C	80	80	0.176
9	B	30	80	0.14
10	C	80	120	0.296
11	B	80	80	0.188
12	B	30	80	0.147
13	B	60	80	0.141
14	A	100	120	0.263
15	A	30	120	0.264
16	B	60	120	0.328
17	C	100	80	0.183
18	C	60	120	0.334
19	C	80	120	0.302
20	A	100	120	0.27
21	C	60	80	0.167
22	A	80	120	0.333
23	A	30	80	0.2
24	A	60	80	0.154
25	B	60	80	0.133
26	B	80	120	0.383
27	A	60	120	0.337
28	B	60	120	0.346
29	C	30	80	0.172
30	B	100	80	0.251
31	C	80	80	0.173
32	C	30	120	0.346
33	A	100	80	0.149
34	B	30	120	0.323
35	B	80	80	0.191
36	C	60	120	0.315
37	B	80	120	0.347
38	C	30	80	0.171
39	B	100	80	0.211
40	A	80	80	0.204
41	A	30	120	0.264
42	A	60	80	0.162
43	A	30	80	0.174
44	C	60	80	0.166
45	C	100	120	0.2
46	A	80	120	0.282
47	C	100	120	0.185
48	B	30	120	0.344

### 3.1. ANOVA Results

The final ANOVA findings for surface roughness (Sa) are shown in Table 6. The ANOVA backward elimination method was used to get rid of the insignificant factors. We first considered all of the model's parameters (direction, layer thickness (LT), and cutting speed (V)) and used backwards to eliminate the one with the highest  $p$ -value. After fitting the new ( $p-1$ ) variable model, we dropped the variable with the highest  $p$ -value. This process persisted until a stopping condition was met. For example, we could have stopped when all the remaining variables had a  $p$ -value of less than 0.05 and the used criterion was the adjusted  $R^2$ . The R-squared, adjusted R-squared, and predicted R-squared values from Table 6 were used to assess the fit of the model. Their closeness to one indicated that the model is adequate. Furthermore, according to Table 6, variable V had a significant impact on surface roughness. Interaction between the LT and V variables occurred next, followed

by direction, LT, and V. Notably, the cutting speed, layer thickness, and direction all play a role in deciding what milling technique to use when working with SS 316L LPBF.

**Table 6.** Analysis of variance for Sa.

Source	DF	Adj SS	Adj MS	F-Value	p-Value
Model	7	0.212360	0.030337	18.89	0.000
Direction	1	0.000284	0.000284	0.18	0.676
LT	1	0.002491	0.002491	1.55	0.220
V	1	0.188084	0.188084	117.10	0.000
Direction * LT	1	0.003679	0.003679	2.29	0.138
Direction * V	1	0.000205	0.000205	0.13	0.723
LT * V	1	0.019560	0.019560	12.18	0.001
Direction * LT * V	1	0.007834	0.007834	4.88	0.033
R-sq = 83.44%		R-sq(adj) = 80.54%		R-sq(pred) = 76.15%	

### 3.2. Optimization of the ANN

This study aimed to develop hybrid algorithms, namely ANN-PSO and ANN-GA, for the optimization of input process settings in the milling process of an additively manufactured part. MATLAB software (MATLAB R2022b.) was used for developing these algorithms with the objective of minimizing surface roughness. The ANN-GA [77] and ANN-PSO [78] Matlab codes were used to obtain the optimal results. For training the ANN, 48 datasets were utilized. Randomly, these 48 datasets were split into 70% training datasets, 15% test datasets, and 15% validation datasets. The ANN results were then implemented in a calculation of the trained network's function for the RMSE and the correlation coefficient ( $R^2$ ). The following subsections describe the tuning parameters and training optimization.

#### 3.2.1. Tuning Parameters of the ANN-GA and ANN-PSO Models

Several metaheuristics, such as the GA and PSO, apply some form of stochastic optimization, which means that the solution found depends on the generated random variables. Therefore, random selection of the ANN-GA and ANN-PSO parameters yields diverse results, and the optimal solution may vary when using the same set of parameters, programming techniques, and computational resources. The tuning parameters were the most important factor in determining the efficiency of the ANN-GA and ANN-PSO algorithms. Consequently, the Taguchi technique was used in this study to find the best combination of parameters for the ANN-PSO and ANN-GA and achieve an optimal solution with minimal randomness.

The initial stage in training with an ANN is the selection of an optimal network structure. Identifying the best configuration of the neural network involves choosing the components of the ANN. These components include selecting the appropriate number of hidden layers and neurons within these layers, as well as identifying the most suitable activation functions and training procedures. In this study, three activation functions, specifically tan-sigmoid, logistic, and purelin, were assessed to identify the optimal network architecture. Additionally, two training algorithms, notably Newton-like and Levenberg–Marquardt, were compared to establish the most effective approach for training the network. Experimental results indicated that the tan-sigmoid function and the purelin function are the most effective activation functions for the middle layers. In addition, the Levenberg–Marquardt algorithm is widely regarded as the most effective learning algorithm.

The GA and PSO parameters, each at five levels, were selected and listed in Table 7 based on the literature and available computational resources. As shown in Table 7, the ANN-GA and ANN-PSO algorithms each contain six and five parameters, respectively, each with five levels. To find the optimal combination of ANN-PSO and ANN-GA parameters, it was necessary to conduct full factorial experiments. The total number of runs were calculated using an easy formula: experiments or runs =  $L^P$ , where  $L$  represents the set of settings or levels, and  $P$  denotes the number of parameters. Therefore, full factorial

experiments, i.e.,  $5^6$  and  $5^5$  or 15,625 and 3125, were performed for the ANN-PSO and ANN-GA. Nevertheless, the L25 orthogonal array table in the Taguchi method is beneficial when determining the ANN-GA and ANN-PSO parameters through 25 experiments and achieving an optimal solution with minimal randomness.

**Table 7.** GA and PSO parameters.

Algorithm	Parameter	Level				
		1	2	3	4	5
ANN-PSO	No. of ANN hidden layers	6	7	8	9	10
	No. of particles	10	20	30	40	50
	Inertia weight	0.1	0.2	0.3	0.7	0.9
	Personal learning coefficient	0.5	1	1.5	2	2.5
	Global learning coefficient	0.5	1	1.5	2	2.5
	No. of iterations	100	150	200	250	300
ANN-GA	No. of hidden layers	6	7	8	9	10
	Population size	50	60	70	80	90
	Crossover percentage	0.2	0.3	0.4	0.5	0.6
	Mutation percentage	0.5	0.6	0.7	0.8	0.9
	No. of iterations	100	150	200	250	300

Figures 5 and 6 illustrate the S/N values of the GA and PSO factors at each level, with the smallest S/N value representing the best level of the GA and PSO parameters. The best ANN-GA parameter setting was 10, 10, 0.1, 1, 0.5, and 150 for the No. of ANN hidden layers, No. of particles, inertia weight, personal learning coefficient, global learning coefficient, and the No. of iterations, respectively. In addition, the best ANN-PSO parameter setting was 8, 50, 0.2, 0.5, and 100 for the number of hidden layers, population size, crossover percentage, mutation percentage, and the number of iterations, respectively.

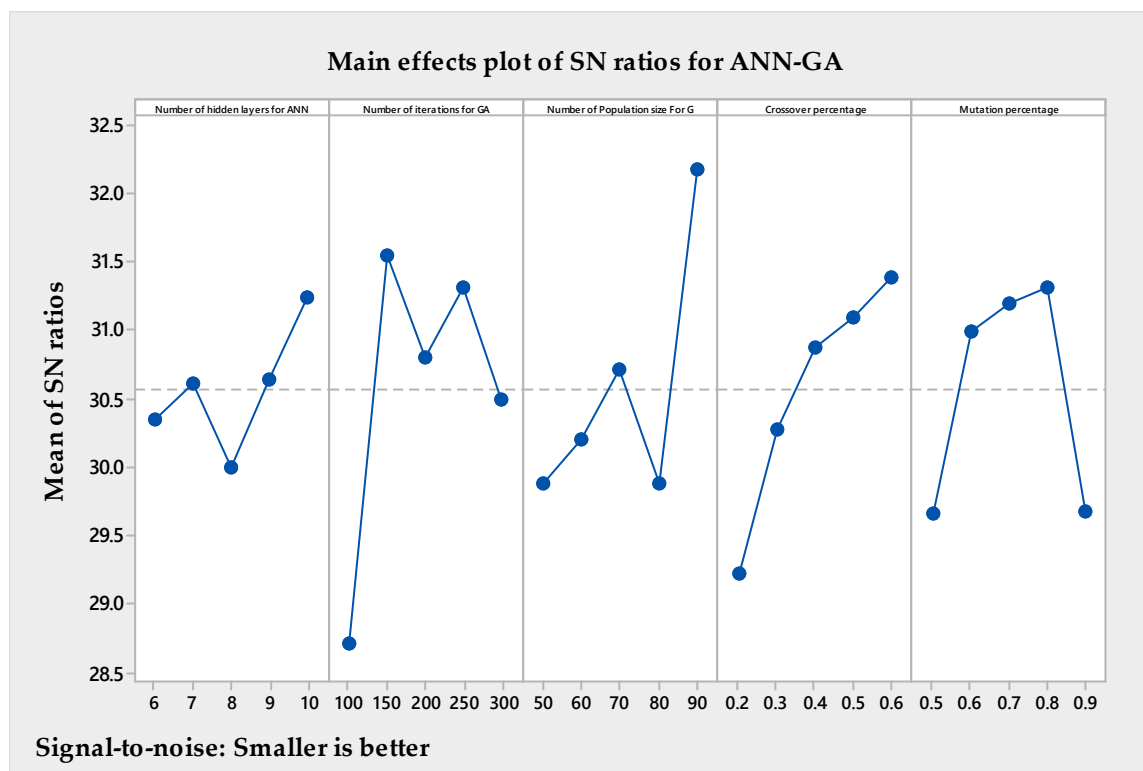


**Figure 5.** Main effects plot of SN ratios for ANN-GA.

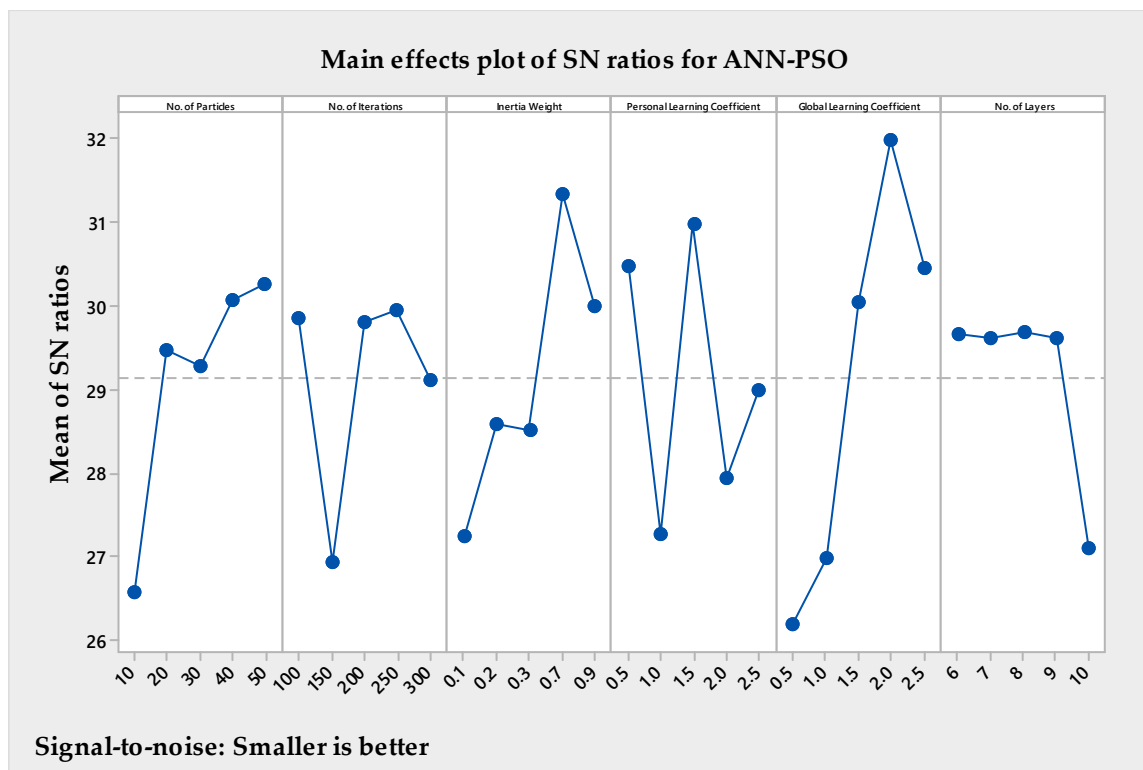


**Figure 6.** Main effects plot of SN ratios for ANN-PSO.

### 3.2.2. Training Optimization of the ANN-GA and ANN-PSO Models

By considering the best parameter settings for the ANN-GA and ANN-PSO algorithms shown in Section 3.2.1, the ANN was trained using 48 datasets of three input process parameters, such as the direction, layer thickness ( $\mu\text{m}$ ), and cutting speed (m/min), and output responses, including the surface roughness ( $\mu\text{m}$ ). The experimental data shown in Table 8 were used to check the performance of the ANN. The performance of these hybrid algorithms was measured using the relative percentage deviation (RPD) of the RMSE. Using the following RPD formulation, the hybrid ANN-PSO and ANN-GA algorithms were evaluated as follows:

$$RPD = \left| \frac{(Pred(i, j) - Exp(i))}{Exp(i)} \right| \quad (6)$$

where  $Pred(i, j)$  is the predicted value obtained via hybrid algorithm  $j$  ( $j = \text{ANN-GA}$  and  $\text{ANN-PSO}$ ) on experiment  $i$ , and  $Exp(i)$  is the value of experiment  $i$ .

Table 8 presents the actual data and data obtained via the ANN-PSO and ANN-GA algorithms to evaluate the performance of the trained ANN. The average RPD was 5.491% for the ANN-GA algorithm, while for the ANN-PSO, the average RPD was 5.605%. The comparison between these values is depicted in chart format in Figures 7 and 8.

As illustrated in Table 9, the  $t$ -test was used to test and compare the RPD values obtained using the ANN-PSO and ANN-GA algorithms. This table presents the error mean, the standard deviation, the standard error mean, the T-value, and the  $p$ -value. The statistical analysis conducted in this study demonstrated that the  $p$ -value associated with the comparison of the mean RPD ANN-GA and the mean RPD ANN-PSO is 0.918, as shown in Table 9. This  $p$ -value indicates that there is no statistically significant difference between the means of these two algorithms. Based on the optimization results, it has been observed that both the hybrid ANN-GA and ANN-PSO algorithms are capable of estimating optimal parameters with a relative percent difference (RPD) of less than 10%. Moreover, we can see

that the average RPD of the ANN-PSO algorithm was greater than that of the ANN-GA algorithm; therefore, the ANN-GA algorithm outperforms the ANN-PSO algorithm.

**Table 8.** Actual and predicted outputs.

Experiment No.	Actual Value	ANN-PSO Predicted Value	ANN-GA Predicted Value	ANN-PSO RPD	ANN-GA RPD
1	0.304	0.212	0.230	0.302	0.244
2	0.204	0.177	0.211	0.132	0.032
3	0.362	0.331	0.339	0.086	0.063
4	0.237	0.237	0.239	0.000	0.009
5	0.146	0.157	0.152	0.073	0.043
6	0.222	0.237	0.239	0.067	0.077
7	0.349	0.355	0.348	0.016	0.004
8	0.176	0.180	0.169	0.021	0.039
9	0.14	0.151	0.158	0.079	0.126
10	0.296	0.289	0.306	0.024	0.033
11	0.188	0.175	0.195	0.070	0.037
12	0.147	0.151	0.158	0.027	0.073
13	0.141	0.137	0.155	0.030	0.096
14	0.263	0.263	0.268	0.000	0.021
15	0.264	0.265	0.269	0.003	0.019
16	0.328	0.348	0.349	0.062	0.064
17	0.183	0.177	0.211	0.032	0.150
18	0.334	0.324	0.317	0.029	0.051
19	0.302	0.289	0.306	0.044	0.012
20	0.27	0.263	0.268	0.026	0.006
21	0.167	0.176	0.154	0.056	0.078
22	0.333	0.326	0.304	0.021	0.088
23	0.2	0.183	0.181	0.087	0.097
24	0.154	0.188	0.166	0.219	0.076
25	0.133	0.137	0.155	0.028	0.162
26	0.383	0.353	0.361	0.077	0.059
27	0.337	0.331	0.339	0.018	0.007
28	0.346	0.348	0.349	0.006	0.009
29	0.172	0.170	0.170	0.012	0.013
30	0.251	0.239	0.226	0.049	0.100
31	0.173	0.180	0.169	0.039	0.023
32	0.346	0.355	0.348	0.025	0.005
33	0.149	0.157	0.152	0.052	0.022
34	0.323	0.329	0.321	0.018	0.005
35	0.191	0.175	0.195	0.084	0.021
36	0.315	0.324	0.317	0.030	0.006
37	0.347	0.353	0.361	0.018	0.039
38	0.171	0.170	0.170	0.006	0.007
39	0.211	0.239	0.226	0.131	0.070
40	0.204	0.212	0.230	0.040	0.127
41	0.264	0.265	0.269	0.003	0.019
42	0.162	0.188	0.166	0.159	0.023
43	0.174	0.183	0.181	0.049	0.039
44	0.166	0.176	0.154	0.062	0.072
45	0.2	0.191	0.180	0.046	0.102
46	0.282	0.326	0.304	0.156	0.077
47	0.185	0.191	0.180	0.032	0.029
48	0.344	0.329	0.321	0.044	0.066

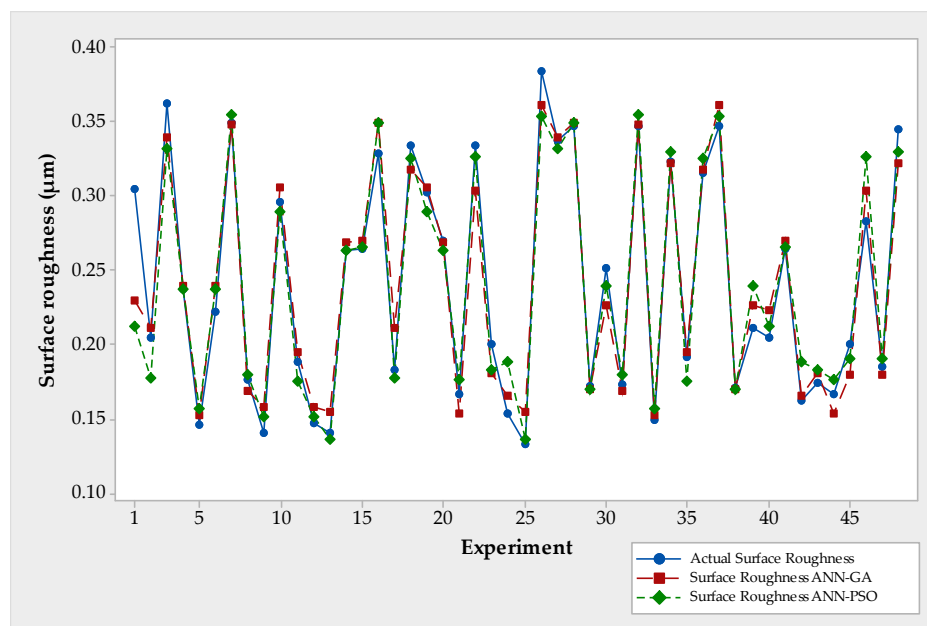


**Figure 7.** Comparison between the actual and predicted values.

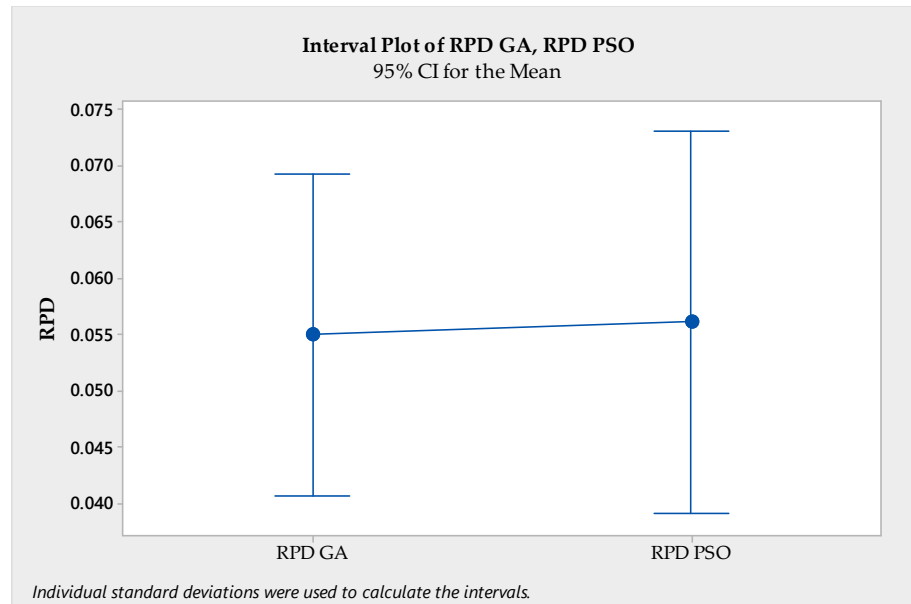


**Figure 8.** Comparison of the RPD GA and RPD PSO.

**Table 9.** Two-sample *t*-test for RPD ANN-GA vs. RPD ANN-PSO.

	N	Mean	StDev	SE Mean	T-Value	p-Value
RPD ANN-GA	48	0.05491	0.04929	0.0071	-0.10	0.918
RPD ANN-PSO	48	0.0560	0.0583	0.0084		

To compare the effectiveness and goodness of fit of the ANN-GA and ANN-PSO algorithms, a hypothesis test was performed, and the results are presented in Table 10. The ANOVA test was used for analyzing the means. The *p*-value observed in the ANOVA table exceeds the significance level of 0.05, indicating that there is no significant evidence to reject the null hypothesis. Consequently, we cannot conclude that there are notable differences between the data obtained from experiments and the data predicted using the ANN-GA

and ANN-PSO algorithms. From a modeling perspective, both hybrid algorithms have a statistically sufficient goodness of fit. Therefore, it can be concluded that the ANN-GA and ANN-PSO algorithms are better at estimating and optimizing the surface roughness of a milling process for an additively manufactured part.

**Table 10.** ANOVA for testing the goodness of fit of the ANN-GA and ANN-PSO algorithms.

	N	Mean	StDev	Individual 95% CI for Mean	F-Value	p-Value
Actual	48	0.2404	0.07672	(0.2181, 0.2627)	0.00	0.999
Predicted ANN-GA	48	0.24007	0.07307	(0.2188, 0.2613)		
Predicted ANN-PSO	48	0.23976	0.07363	(0.2184, 0.2611)		

Figure 9 illustrates a regression analysis of the data, highlighting the linear coefficient of correlation ( $R$ ) during the training, testing, and validation stages. Based on the results presented in Figure 9, it is obvious that the Levenberg–Marquardt algorithm yielded the highest  $R$  value (0.97333) when applied to the whole data. As a result, the ANN generated empty circles in contrast to the target values, while dashed lines represent the ideal linear approximation. The closeness of the fitted line to the midpoint shows that the neural network was able to estimate surface roughness values using different input process parameters in the milling process of an additively made component. Throughout the training process, the data achieved its highest level of optimization at the seventh iteration. At this point, the validation sample's RMSE started to increase. Consequently, the training epochs were immediately terminated. This observation is depicted in Figure 10, which displays the plot of the RMSE. During epoch 3, the highest level of validation performance achieved was  $5.2522 \times 10^{-4}$ .

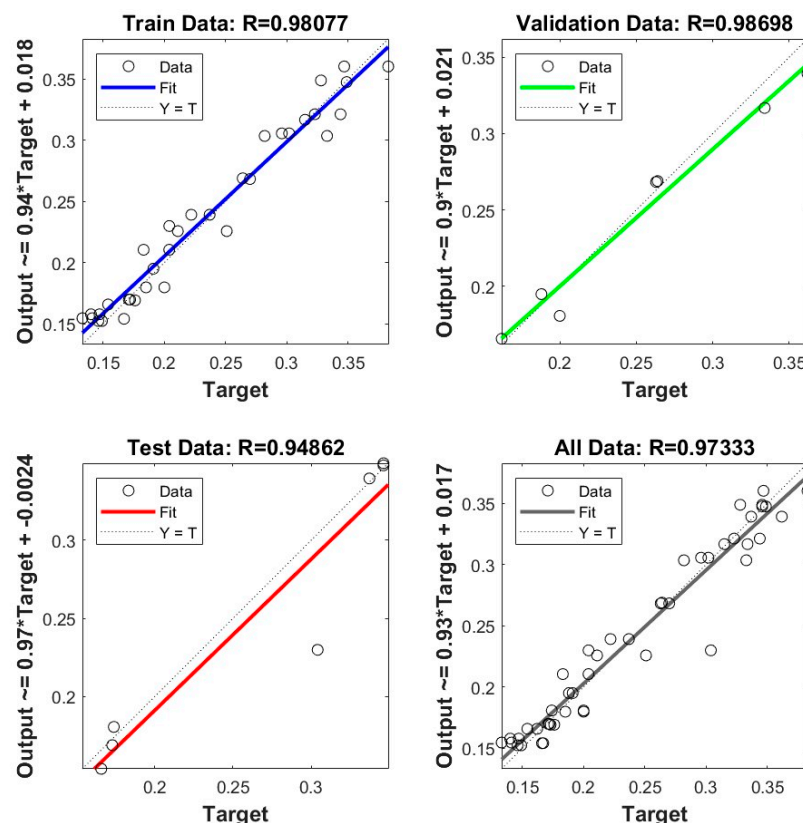


**Figure 9.** A plot of regression for the ANN-PSO.

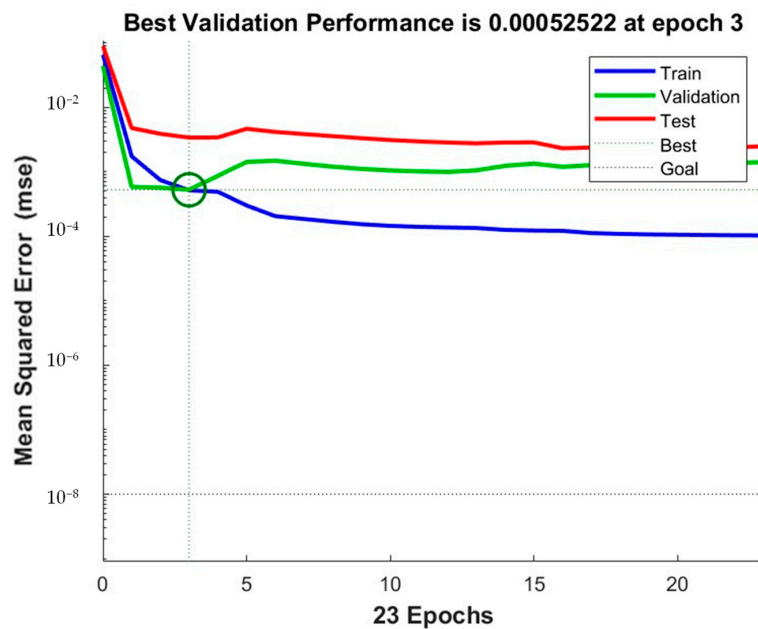


**Figure 10.** A plot of mean square error for the ANN-PSO.

The ANN-PSO parameters were chosen as the number of hidden layers: 9, population size: 90, crossover percentage: 0.4, mutation percentage: 0.5, and stopping criteria: 150 iterations. Based on the experimental matrix, the minimal surface roughness was 0.133  $\mu\text{m}$  when the input process parameters were attained as face B, 60  $\mu\text{m}$  layer thickness, and 80 m/min cutting speed, while the optimization result considering the previous ANN-PSO parameters was 0.137  $\mu\text{m}$ . As a consequence, the ANN-PSO algorithm improved the surface quality. Figure 11 illustrates the improvement in surface quality of the components achieved through the implementation of optimization methods.

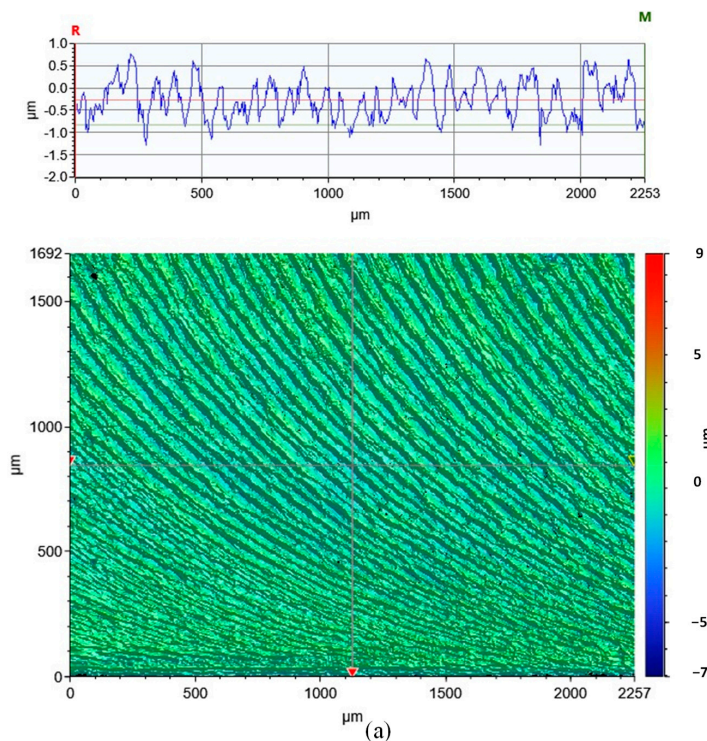


**Figure 11. Cont.**

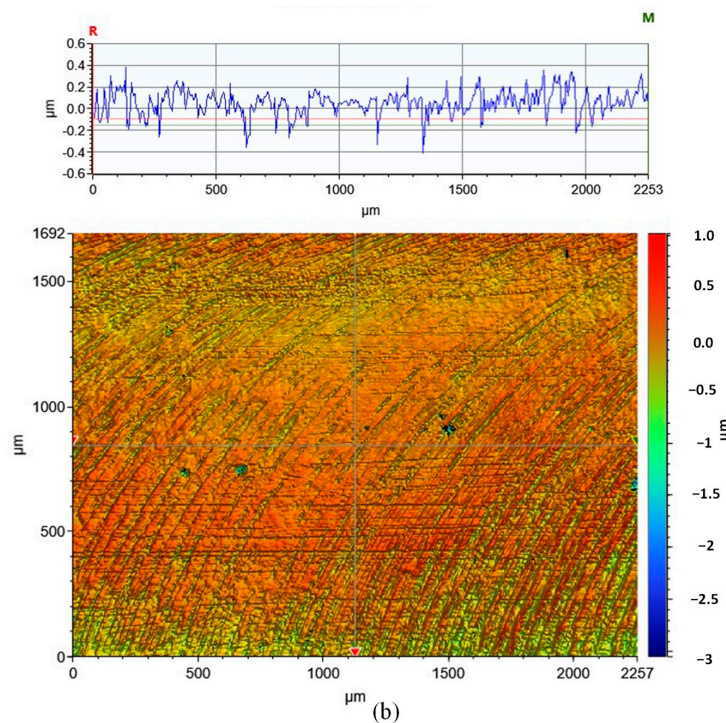


**Figure 11.** Surface quality samples (a) before optimization (surface roughness = 0.383  $\mu\text{m}$ ) and (b) after optimization (surface roughness = 0.133  $\mu\text{m}$ ).

#### 4. Conclusions

This study investigates the effect of input process settings on the milling process of a part produced via additive manufacturing. In this investigation, a total of 48 experiments were designed after the identification of the range of input process parameters. This study aimed to explore the impact of input parameters, namely the direction, layer thickness ( $\mu\text{m}$ ), and cutting speed ( $\text{m}/\text{min}$ ), on the surface roughness ( $\mu\text{m}$ ) of components using a full factorial design.

The main objective of this study was to find the optimal settings for obtaining the highest possible surface quality. In order to optimize the milling process conditions of a component manufactured via additive manufacturing, a comprehensive approach was developed. This approach involves the utilization of a full factorial design, as well as the integration of hybrid algorithms that combine neural networks with genetic algorithms and particle swarm optimization. Consequently, the experimental matrix was subsequently consolidated to the training process in order to identify the most optimal combination of input parameters through the utilization of hybrid algorithms. The optimal parameters for model validation have been systematically collected and analyzed.

Based on the experimental data, it can be seen that the minimum surface roughness achieved was 0.133  $\mu\text{m}$ . Further optimization techniques were applied, resulting in surface roughness values of 0.155  $\mu\text{m}$  for the ANN-GA approach and 0.137  $\mu\text{m}$  for the ANN-PSO. Consequently, both ANN-GA and ANN-PSO have improved surface quality, and they are more effective in this regard. Hence, the use of meta-heuristic algorithms optimizes the performance of the milling process parameters of an additively manufactured part. Finally, Figure 11 illustrates the improvement in surface quality of the components achieved through the implementation of optimization techniques.

**Author Contributions:** Conceptualization, A.D. and H.K.; methodology, A.D., H.K. and E.H.A.; validation, A.D., S.A. and A.Y.A.; formal analysis, H.K., A.D. and K.N.A.; investigation, A.D., S.A., A.M.A.-S. and A.Y.A.; data curation, A.D., H.K. and K.N.A.; writing—original draft preparation, A.D. and H.K.; writing—review and editing, K.N.A. and E.H.A.; visualization, A.D., S.A., A.M.A.-S. and

A.Y.A.; supervision, S.A. and A.M.A.-S.; resources, E.H.A. and K.N.A. All authors have read and agreed to the published version of the manuscript.

**Funding:** The researchers were supported by project number RC442/50, Taibah University, Medinah, Saudi Arabia.

**Data Availability Statement:** All data generated or analyzed during this study are included in the present article.

**Acknowledgments:** The authors extend their appreciation to Taibah University, represented by the Deanship of Scientific Research, for funding this project (No. RC-442/50).

**Conflicts of Interest:** The authors declare no conflict of interest.

## References

1. Serda, M.; Becker, F.G.; Cleary, M.; Team, R.M.; Holtermann, H.; The, D.; Agenda, N.; Science, P.; Sk, S.K.; Hinnebusch, R.; et al. Machinability of Aisi 410 Martensitic Stainless Steels Depending on Cutting Tool and Coating. *J. Fac. Eng. Archit. GAZI Univ.* **2009**, *24*, 343–354. [[CrossRef](#)]
2. Kara, F.; Aslantas, K.; Çiçek, A. ANN and Multiple Regression Method-Based Modelling of Cutting Forces in Orthogonal Machining of AISI 316L Stainless Steel. *Neural Comput. Appl.* **2015**, *26*, 237–250. [[CrossRef](#)]
3. Elthalabawy, W.M.; Khan, T.I. Eutectic Bonding of Austenitic Stainless Steel 316L to Magnesium Alloy AZ31 Using Copper Interlayer. *Int. J. Adv. Manuf. Technol.* **2011**, *55*, 235–241. [[CrossRef](#)]
4. Chang, L.; Mukahiwa, K.; Volpe, L.; Scenini, F. Effect of Machining on Oxide Development in Type 316L Stainless Steel in High-Temperature Hydrogenated Water. *Corros. Sci.* **2021**, *186*, 109444. [[CrossRef](#)]
5. Gurappa, I. Characterization of Different Materials for Corrosion Resistance under Simulated Body Fluid Conditions. *Mater. Charact.* **2002**, *49*, 73–79. [[CrossRef](#)]
6. Sultan, A.Z.; Sharif, S.; Kurniawan, D. Effect of Machining Parameters on Tool Wear and Hole Quality of AISI 316L Stainless Steel in Conventional Drilling. *Procedia Manuf.* **2015**, *2*, 202–207. [[CrossRef](#)]
7. Kumar, P.S.; Acharyya, S.G.; Rao, S.V.R.; Kapoor, K. Distinguishing Effect of Buffing vs. Grinding, Milling and Turning Operations on the Chloride Induced SCC Susceptibility of 304L Austenitic Stainless Steel. *Mater. Sci. Eng. A* **2017**, *687*, 193–199. [[CrossRef](#)]
8. Umbrello, D.; Filice, L. Improving Surface Integrity in Orthogonal Machining of Hardened AISI 52100 Steel by Modeling White and Dark Layers Formation. *CIRP Ann.* **2009**, *58*, 73–76. [[CrossRef](#)]
9. Zhou, N.; Pettersson, R.; Peng, R.L.; Schöning, M. Effect of Surface Grinding on Chloride Induced SCC of 304L. *Mater. Sci. Eng. A* **2016**, *658*, 50–59. [[CrossRef](#)]
10. Sing, S.L.; An, J.; Yeong, W.Y.; Wiria, F.E. Laser and Electron-Beam Powder-Bed Additive Manufacturing of Metallic Implants: A Review on Processes, Materials and Designs. *J. Orthop. Res.* **2016**, *34*, 369–385. [[CrossRef](#)]
11. Wang, D.; Liu, Y.; Yang, Y.; Xiao, D. Theoretical and Experimental Study on Surface Roughness of 316L Stainless Steel Metal Parts Obtained through Selective Laser Melting. *Rapid Prototyp. J.* **2016**, *22*, 706–716. [[CrossRef](#)]
12. Liu, Y.J.; Wang, H.L.; Li, S.J.; Wang, S.G.; Wang, W.J.; Hou, W.T.; Hao, Y.L.; Yang, R.; Zhang, L.C. Compressive and Fatigue Behavior of Beta-Type Titanium Porous Structures Fabricated by Electron Beam Melting. *Acta Mater.* **2017**, *126*, 58–66. [[CrossRef](#)]
13. Kaynak, Y.; Kitay, O. Porosity, Surface Quality, Microhardness and Microstructure of Selective Laser Melted 316L Stainless Steel Resulting from Finish Machining. *J. Manuf. Mater. Process.* **2018**, *2*, 36. [[CrossRef](#)]
14. Li, R.; Liu, J.; Shi, Y.; Du, M.; Xie, Z. 316L Stainless Steel with Gradient Porosity Fabricated by Selective Laser Melting. *J. Mater. Eng. Perform.* **2010**, *19*, 666–671. [[CrossRef](#)]
15. Spierings, A.B.; Levy, G. Comparison of Density of Stainless Steel 316L Parts Produced with Selective Laser Melting Using Different Powder Grades. 2009. Available online: <https://repositories.lib.utexas.edu/handle/2152/88172> (accessed on 12 June 2023).
16. Stamp, R.; Fox, P.; O'Neill, W.; Jones, E.; Sutcliffe, C. The Development of a Scanning Strategy for the Manufacture of Porous Biomaterials by Selective Laser Melting. *J. Mater. Sci. Mater. Med.* **2009**, *20*, 1839–1848. [[CrossRef](#)]
17. Riemer, A.; Leuders, S.; Richard, H.A.; Tröster, T.; Riemer, A.; Leuders, S.; Thöne, M.; Richard, H.A.; Tröster, T.; Niendorf, T. On the Fatigue Crack Growth Behavior in 316L Stainless Steel Manufactured by Selective Laser Melting. *Eng. Fract. Mech.* **2014**, *120*, 15–25. [[CrossRef](#)]
18. Yasa, E.; Kruth, J.P. Microstructural Investigation of Selective Laser Melting 316L Stainless Steel Parts Exposed to Laser Re-Melting. *Procedia Eng.* **2011**, *19*, 389–395. [[CrossRef](#)]
19. Yasa, E.; Kruth, J.P.; Deckers, J. Manufacturing by Combining Selective Laser Melting and Selective Laser Erosion/Laser Re-Melting. *CIRP Ann. Manuf. Technol.* **2011**, *60*, 263–266. [[CrossRef](#)]
20. Strano, G.; Hao, L.; Everson, R.M.; Evans, K.E. Surface Roughness Analysis, Modelling and Prediction in Selective Laser Melting. *J. Mater. Process. Technol.* **2013**, *213*, 589–597. [[CrossRef](#)]
21. Delgado, J.; Ciurana, J.; Rodríguez, C.A. Influence of Process Parameters on Part Quality and Mechanical Properties for DMLS and SLM with Iron-Based Materials. *Int. J. Adv. Manuf. Technol.* **2012**, *60*, 601–610. [[CrossRef](#)]

22. Nguyen, Q.B.; Luu, D.N.; Nai, S.M.L.; Zhu, Z.; Chen, Z.; Wei, J. The Role of Powder Layer Thickness on the Quality of SLM Printed Parts. *Arch. Civ. Mech. Eng.* **2018**, *18*, 948–955. [[CrossRef](#)]
23. Lou, X.; Othon, M.A.; Rebak, R.B. Corrosion Fatigue Crack Growth of Laser Additively-Manufactured 316L Stainless Steel in High Temperature Water. *Corros. Sci.* **2017**, *127*, 120–130. [[CrossRef](#)]
24. de Souza, A.F.; Al-Rubaie, K.S.; Marques, S.; Zluhan, B.; Santos, E.C. Effect of Laser Speed, Layer Thickness, and Part Position on the Mechanical Properties of Maraging 300 Parts Manufactured by Selective Laser Melting. *Mater. Sci. Eng. A* **2019**, *767*, 138425. [[CrossRef](#)]
25. Tian, Y.; Tomus, D.; Rometsch, P.; Wu, X. Influences of Processing Parameters on Surface Roughness of Hastelloy X Produced by Selective Laser Melting. *Addit. Manuf.* **2017**, *13*, 103–112. [[CrossRef](#)]
26. Guo, C.; Li, S.; Shi, S.; Li, X.; Hu, X.; Zhu, Q.; Ward, R.M. Effect of Processing Parameters on Surface Roughness, Porosity and Cracking of as-Built IN738LC Parts Fabricated by Laser Powder Bed Fusion. *J. Mater. Process. Technol.* **2020**, *285*, 116788. [[CrossRef](#)]
27. Zhang, B.; Ziegert, J.; Farahi, F.; Davies, A. In Situ Surface Topography of Laser Powder Bed Fusion Using Fringe Projection. *Addit. Manuf.* **2016**, *12*, 100–107. [[CrossRef](#)]
28. Yeung, H.; Lane, B.; Fox, J. Part Geometry and Conduction-Based Laser Power Control for Powder Bed Fusion Additive Manufacturing. *Addit. Manuf.* **2019**, *30*, 100844. [[CrossRef](#)]
29. Al-Rubaie, K.S.; Mario Fernandes Paiva, J.J.; Veldhuis, S.; Melotti, S.; Rabelo, A.; Paiva, J.M.; Elbestawi, M.A.; Veldhuis, S.C. Machinability of SLM-Produced Ti6Al4V Titanium Alloy Parts. *Artic. J. Manuf. Process.* **2020**, *57*, 768–786. [[CrossRef](#)]
30. Dabwan, A.; Anwar, S.; Al-Samhan, A.M.; AlFaify, A.; Nasr, M.M. Investigations on the Effect of Layers' Thickness and Orientations in the Machining of Additively Manufactured Stainless Steel 316L. *Materials* **2021**, *14*, 1797. [[CrossRef](#)]
31. Lebon, N.; Tapie, L.; Vennat, E.; Mawussi, B. Influence of CAD/CAM Tool and Material on Tool Wear and Roughness of Dental Prostheses after Milling. *J. Prosthet. Dent.* **2015**, *114*, 236–247. [[CrossRef](#)]
32. Bordin, A.; Bruschi, S.; Ghiotti, A.; Bucciotti, F.; Facchini, L. Comparison between Wrought and EBM Ti6Al4V Machinability Characteristics. *Key Eng. Mater.* **2014**, *611–612*, 1186–1193. [[CrossRef](#)]
33. Anwar, S.; Ahmed, N.; Abdo, B.M.; Pervaiz, S.; Chowdhury, M.A.K.; Alahmari, A.M. Electron Beam Melting of Gamma Titanium Aluminide and Investigating the Effect of EBM Layer Orientation on Milling Performance. *Int. J. Adv. Manuf. Technol.* **2018**, *96*, 3093–3107. [[CrossRef](#)]
34. Anwar, S.; Ahmed, N.; Pervaiz, S.; Ahmad, S.; Mohammad, A.; Saleh, M. On the Turning of Electron Beam Melted Gamma-TiAl with Coated and Uncoated Tools: A Machinability Analysis. *J. Mater. Process. Technol.* **2020**, *282*, 116664. [[CrossRef](#)]
35. Polishetty, A.; Nomani, J.; Littlefair, G. Evaluating and Comparing Secondary Machining Characteristics of Wrought and Additive Manufactured 316L Stainless Steel. *Mater. Today Proc.* **2023**, in press. [[CrossRef](#)]
36. Farooq, M.U.; Anwar, S.; Ullah, R.; Guerra, R.H. Sustainable Machining of Additive Manufactured SS-316L Underpinning Low Carbon Manufacturing Goal. *J. Mater. Res. Technol.* **2023**, *24*, 2299–2318. [[CrossRef](#)]
37. Struzikiewicz, G.; Zębala, W.; Matras, A.; Machno, M.; Ślusarczyk, Ł.; Hichert, S.; Laufer, F. Turning Research of Additive Laser Molten Stainless Steel 316L Obtained by 3D Printing. *Materials* **2019**, *12*, 182. [[CrossRef](#)]
38. Alqahtani, K.N.; Dabwan, A.; Abualsauod, E.H.; Anwar, S. Multi-Response Optimization of Additively Manufactured Ti6Al4V Component Using Grey Relational Analysis Coupled with Entropy Weights. *Metals* **2023**, *13*, 1130. [[CrossRef](#)]
39. Dabwan, A.; Anwar, S.; Al-Samhan, A.M.; Alqahtani, K.N.; Nasr, M.M.; Kaid, H.; Ameen, W. CNC Turning of an Additively Manufactured Complex Profile Ti6Al4V Component Considering the Effect of Layer Orientations. *Processes* **2023**, *11*, 1031. [[CrossRef](#)]
40. Dabwan, A.; Anwar, S.; Al-Samhan, A.M.; Nasr, M.M. On the Effect of Electron Beam Melted Ti6Al4V Part Orientations during Milling. *Metals* **2020**, *10*, 1172. [[CrossRef](#)]
41. Dabwan, A.; Anwar, S.; Al-Samhan, A.M.; Nasr, M.M.; AlFaify, A. On the Influence of Heat Treatment in Suppressing the Layer Orientation Effect in Finishing of Electron Beam Melted Ti6Al4V. *Int. J. Adv. Manuf. Technol.* **2022**, *118*, 3035–3048. [[CrossRef](#)]
42. Khorasani, A.M.; Yazdi, M.R.S. Development of a Dynamic Surface Roughness Monitoring System Based on Artificial Neural Networks (ANN) in Milling Operation. *Int. J. Adv. Manuf. Technol.* **2017**, *93*, 141–151. [[CrossRef](#)]
43. Kant, G.; Singh, K. Predictive Modelling and Optimization of Machining Parameters to Minimize Surface Roughness Using Artificial Neural Network Coupled with Genetic Algorithm. *Procedia CIRP* **2015**, *31*, 453–458. [[CrossRef](#)]
44. El-Bahloul, S.A. Optimization of Wire Electrical Discharge Machining Using Statistical Methods Coupled with Artificial Intelligence Techniques and Soft Computing. *SN Appl. Sci.* **2020**, *2*, 49. [[CrossRef](#)]
45. Sivagurumanikandan, N.; Saravanan, S.; Kumar, G.S.; Raju, S.; Raghukandan, K. Prediction and Optimization of Process Parameters to Enhance the Tensile Strength of Nd: YAG Laser Welded Super Duplex Stainless Steel. *Optik* **2018**, *157*, 833–840. [[CrossRef](#)]
46. Turkson, R.F.; Yan, F.; Ali, M.K.A.; Hu, J. Artificial Neural Network Applications in the Calibration of Spark-Ignition Engines: An Overview. *Eng. Sci. Technol. Int. J.* **2016**, *19*, 1346–1359. [[CrossRef](#)]
47. Yadav, D.; Chhabra, D.; Kumar Garg, R.; Ahlawat, A.; Phogat, A. Optimization of FDM 3D Printing Process Parameters for Multi-Material Using Artificial Neural Network. *Mater. Today Proc.* **2020**, *21*, 1583–1591. [[CrossRef](#)]
48. Giri, J.; Shahane, P.; Jachak, S.; Chadge, R.; Giri, P. Optimization of Fdm Process Parameters for Dual Extruder 3d Printer Using Artificial Neural Network. *Mater. Today Proc.* **2021**, *43*, 3242–3249. [[CrossRef](#)]

49. Shirmohammadi, M.; Goushchi, S.J.; Keshtiban, P.M. Optimization of 3D Printing Process Parameters to Minimize Surface Roughness with Hybrid Artificial Neural Network Model and Particle Swarm Algorithm. *Prog. Addit. Manuf.* **2021**, *6*, 199–215. [[CrossRef](#)]
50. Soler, D.; Telleria, M.; García-Blanco, M.B.; Espinosa, E.; Cuesta, M.; Arrazola, P.J. Prediction of Surface Roughness of SLM Built Parts after Finishing Processes Using an Artificial Neural Network. *J. Manuf. Mater. Process.* **2022**, *6*, 82. [[CrossRef](#)]
51. Saad, M.S.; Mohd Nor, A.; Abd Rahim, I.; Syahruddin, M.A.; Mat Darus, I.Z. Optimization of FDM Process Parameters to Minimize Surface Roughness with Integrated Artificial Neural Network Model and Symbiotic Organism Search. *Neural Comput. Appl.* **2022**, *34*, 17423–17439. [[CrossRef](#)]
52. AlFaify, A.; Hughes, J.; Ridgway, K. Controlling the Porosity of 316L Stainless Steel Parts Manufactured via the Powder Bed Fusion Process. *Rapid Prototyp. J.* **2019**, *25*, 162–175. [[CrossRef](#)]
53. Grguraš, D.; Kern, M. Cutting Performance of Solid Ceramic and Carbide End Milling Tools in Machining of Nickel Based Alloy Inconel 718 and Stainless Steel 316L. *Adv. Prod. Eng. Manag.* **2019**, *14*, 27–38. [[CrossRef](#)]
54. Khleif, A.A. Effect of Cutting Parameters on Wear and Surface Roughness of Stainless Steel (316L) Using Milling Process. *Al-Nahrain Univ. Coll. Eng. J.* **2016**, *91*, 286–292.
55. Yasir, M.; Ginta, T.L.; Ariwahjoedi, B.; Alkali, A.U.; Danish, M. Effect of Cutting Speed and Feed Rate on Surface Roughness of AISI 316L SS Using End-Milling. *ARPN J. Eng. Appl. Sci.* **2016**, *11*, 2496–2500.
56. Wade, S.A.; Javed, M.A.; Palombo, E.A.; McArthur, S.L.; Stoddart, P.R. On the Need for More Realistic Experimental Conditions in Laboratory-Based Microbiologically Influenced Corrosion Testing. *Int. Biodeterior. Biodegrad.* **2017**, *121*, 97–106. [[CrossRef](#)]
57. Heinl, M.; Heinl, M.; Greiner, S.; Wudy, K.; Pobel, C.; Rasch, M.; Rasch, M.; Huber, F.; Huber, F.; Papke, T.; et al. Measuring Procedures for Surface Evaluation of Additively Manufactured Powder Bed-Based Polymer and Metal Parts. *Meas. Sci. Technol.* **2020**, *31*, 095202. [[CrossRef](#)]
58. Gravano, A. Turn-Taking and Affirmative Cue Words in Task-Oriented Dialogue. *Diss. Abstr. Int. B Sci. Eng.* **2010**, *70*, 4943. [[CrossRef](#)]
59. Goldberg, Y.; Liu, Y.; Zhang, M. Neural Network Methods for Natural Language Processing. *Comput. Linguist.* **2018**, *44*, 193–195. [[CrossRef](#)]
60. Rumelhart, D.E.; Hinton, G.E.; Williams, R.J. Learning Representations by Back-Propagating Errors. *Nature* **1986**, *323*, 533–536. [[CrossRef](#)]
61. Pimenov, D.Y.; Bustillo, A.; Mikolajczyk, T. Artificial Intelligence for Automatic Prediction of Required Surface Roughness by Monitoring Wear on Face Mill Teeth. *J. Intell. Manuf.* **2018**, *29*, 1045–1061. [[CrossRef](#)]
62. Lin, Y. *Neural Networks in Bioprocessing and Chemical Engineering*; Elsevier: Amsterdam, The Netherlands, 2014.
63. Ghanbari, F.; Modirshahla, N.; Khosravi, M.; Behnajady, M.A. Synthesis of TiO<sub>2</sub> Nanoparticles in Different Thermal Conditions and Modeling Its Photocatalytic Activity with Artificial Neural Network. *J. Environ. Sci.* **2012**, *24*, 750–756. [[CrossRef](#)]
64. Cao, R.; Fan, M.; Hu, J.; Ruan, W.; Wu, X.; Wei, X. Artificial Intelligence Based Optimization for the Se(IV) Removal from Aqueous Solution by Reduced Graphene Oxide-Supported Nanoscale Zero-Valent Iron Composites. *Materials* **2018**, *11*, 428. [[CrossRef](#)]
65. Azadeh, A.; Ghaderi, S.F.; Tarverdian, S.; Saberi, M. Integration of Artificial Neural Networks and Genetic Algorithm to Predict Electrical Energy Consumption. *Appl. Math. Comput.* **2007**, *186*, 1731–1741. [[CrossRef](#)]
66. Li, K.; Thompson, S.; Wieringa, P.A.; Peng, J.; Duan, G.R. Neural Networks and Genetic Algorithms Can Support Human Supervisory Control to Reduce Fossil Fuel Power Plant Emissions. *Cogn. Technol. Work* **2003**, *5*, 107–126. [[CrossRef](#)]
67. Momeni, E.; Jahed Armaghani, D.; Hajihassani, M.; Mohd Amin, M.F. Prediction of Uniaxial Compressive Strength of Rock Samples Using Hybrid Particle Swarm Optimization-Based Artificial Neural Networks. *Measurement* **2015**, *60*, 50–63. [[CrossRef](#)]
68. Meissner, M.; Schmuker, M.; Schneider, G. Optimized Particle Swarm Optimization (OPSO) and Its Application to Artificial Neural Network Training. *BMC Bioinform.* **2006**, *7*, 125. [[CrossRef](#)]
69. Geethanjali, M.; Raja Slochanal, S.M.; Bhavani, R. PSO Trained ANN-Based Differential Protection Scheme for Power Transformers. *Neurocomputing* **2008**, *71*, 904–918. [[CrossRef](#)]
70. Khayat, O.; Ebadzadeh, M.M.; Shahroostei, H.R.; Rajaei, R.; Khajehnasiri, I. A Novel Hybrid Algorithm for Creating Self-Organizing Fuzzy Neural Networks. *Neurocomputing* **2009**, *73*, 517–524. [[CrossRef](#)]
71. Jaddi, N.S.; Abdullah, S.; Hamdan, A.R. Optimization of Neural Network Model Using Modified Bat-Inspired Algorithm. *Appl. Soft Comput.* **2015**, *37*, 71–86. [[CrossRef](#)]
72. Holland, J. *Adaptation in Natural and Artificial Systems: An Introductory Analysis with Applications to Biology, Control, and Artificial Intelligence*; MIT Press: Cambridge, MA, USA, 1992.
73. Sivanandam, S.N.; Deepa, S.N. Genetic Algorithms. In *Introduction to Genetic Algorithms*; Springer: Berlin/Heidelberg, Germany, 2008; pp. 15–37. [[CrossRef](#)]
74. Mirjalili, S. *Evolutionary Algorithms and Neural Networks*; Springer: Cham, Switzerland, 2019; Volume 780. [[CrossRef](#)]
75. Kennedy, J.; Eberhart, R. Particle Swarm Optimization. In Proceedings of the ICNN'95—International Conference on Neural Networks, Perth, WA, Australia, 27 November–1 December 1995.
76. Tyagi, K.; Tyagi, K. A Comparative Analysis of Optimization Techniques. *Int. J. Comput. Appl.* **2015**, *131*, 6–12. [[CrossRef](#)]

77. Ghasri, M. Hybrid Artificial Neural Network with Genetic Algorithm. MATLAB Central File Exchange. Available online: <https://www.Mathworks.Com/Matlabcentral/Fileexchange/124600-Hybrid-Artificial-Neural-Network-with-Genetic-Algorithm> (accessed on 24 August 2023).
78. Selva. Particle Swarm Optimized Neural Network. MATLAB Central File Exchange. Available online: <https://www.Mathworks.Com/Matlabcentral/Fileexchange/64371-Particle-Swarm-Optimized-Neural-Network> (accessed on 24 August 2023).

**Disclaimer/Publisher's Note:** The statements, opinions and data contained in all publications are solely those of the individual author(s) and contributor(s) and not of MDPI and/or the editor(s). MDPI and/or the editor(s) disclaim responsibility for any injury to people or property resulting from any ideas, methods, instructions or products referred to in the content.